Sulfuric Acid Degradation of Alkali-Activated Metakaolin Cements Supplemented with Brucite

Juan Pablo Gevaudan [1], Zoey Craun[1], Wil V. Srubar III [1,2,†]

[1]Department of Civil, Environmental, and Architectural Engineering, University of Colorado Boulder, Boulder, Colorado USA. [2]Materials Science and Engineering Program, University of Colorado Boulder, Boulder, Colorado USA. [†]Corresponding Author 1111 Engineering Drive, ECOT 441 UCB 428, Boulder, Colorado USA 80309. T +1 303 492 2621, E: wsrubar@colorado.edu

Abstract

This study investigated the effect of alkali content (Na:Al = 0.86 and 1.39) and brucite (*i.e.*, $Mg(OH)_2$) mineral addition on the sulfuric acid resistance of alkali-activated metakaolin (*i.e.*, geopolymers). Geopolymers consist primarily of a sodium-stabilized aluminosilicate hydrate (N-A-S-H) framework. Results demonstrate that higher alkali contents and brucite addition improves the acid resistance of N-A-S-H, as evidenced by reduced dealumination and Si and Na leaching upon exposure to acid. These results are mechanistically explained by increased retention of Mg^{2+} within the microstructure and increased Mg-Al interaction upon acid exposure. Higher Mg^{2+} retention and increased Mg-Al coupling together provide empirical evidence of *polyvalent cationic stabilization*—a mechanism involving polyvalent cations (*e.g.*, Mg^{2+}) that stabilize the N-A-S-H binder by arresting acid-induced electrophilic attack. Results further illustrate that brucite addition, especially at high-alkali content formulations, reduces micro-scale porosity while increasing the proportion of gel pores (< 5nm), which suggests that increased

tortuosity of gel pores may aid in Mg^{2+} retention and promote the increased Mg-Al coupling observed herein.

Keywords: Alkali-activated materials, geopolymers, acid attack, mineral admixtures, pore structure

1. Introduction

Calcium-free (Ca-free) alkali-activated cements (AACs), also named geopolymers, are primarily composed of sodium-stabilized aluminosilicate hydrate (N-A-S-H) gels. These cementitious binders can offer multiple benefits in terms of low-CO_2 emissions and durability properties compared to portland cement [1–3]. Alkali-activation of an aluminosilicate material (*e.g.*, metakaolin) begins with precursor dissolution in a high-pH activator solution, which releases silica and alumina species [4]. As the precursor dissolves, silicate and alumina species polymerize to form a cation-stabilized cementitious binder [5]. In Ca-free AACs, the main binder comprises an amorphous N-A-S-H cementitious binder [6]. Lower Ca contents of N-A-S-H materials have been linked to improved durability performance, namely for sulfate and seawater attack, acid exposure, alkali-silica reaction, steel corrosion, and fire [7].

Biogenic acid corrosion of concrete structures is a major cause of civil infrastructure deterioration. Corrosion due to sulfuric acid is the most common form of this mechanism [8]. Previous studies have shown that AACs are more resistant to acid attack than ordinary portland cement (OPC) [9] [10]. Briefly, the acid degradation of calcium-free AACs begins with an ion-exchange between framework cations (*i.e.*, sodium) and protons from the acid solution. The protons induce an electrophilic attack, which results in the ejection of aluminum (*i.e.*, dealumination) from the Si-O-Al bonds of the binder [11].

The complex mechanisms of acid deterioration of Ca-free AACs are not well understood. Further research is needed to be able to better predict dissolution-precipitation reactions of the AAC binders, while taking into consideration different factors, such as Si:Al ratios and varying H_2O and cation contents [12]. In addition, more research is required to understand how mineral phases—either unreacted minerals or minerals precipitated during alkali activation—affect acid degradation [13–15]. The availability of network-modifying cations, such as magnesium (*i.e.*, Mg^{2+}), can affect the durability of AACs by influencing microstructural changes occurring within the N-A-S-H gel either (1) during alkali activation or (2) upon exposure to acid. Previous research has shown that minerals can provide multivalent cations, like Mg^{2+}, have the potential to improve the acid resistance of AACs by stabilizing the gel at the acid degradation front [16,17]. However, the chemical heterogeneity, polycrystallinity, and variability of many industrial aluminosilicates that are used as precursors for alkali-activation (*e.g.*, slag, fly ash) confound the mechanistic understanding of the role of Mg^{2+} in acid degradation of AACs.

Brucite is a common mineral present in industrial aluminosilicate precursors used in the production of AACs, such as high-magnesium and high-nickel slag and, to a lower extent, natural clays (*e.g.*, bentonite). Brucite can also form as a result of alkali-activation, since it is thermodynamically favorable to form under Al-deficient conditions that can exist during slag activation [18–20]. Hence, due to its common presence in AACs and its solubility at low pH (*i.e.*, acidic) conditions, it is important to understand the effect of brucite—and Mg^{2+} specifically—on the acid resistance of AACs. In this study, metakaolin was selected as the aluminosilicate precursor due to the purity of its aluminosilicate chemical composition, high reactivity, and proven ability to form N-A-S-H. By utilizing metakaolin, we consequently aim to isolate the role of Mg^{2+} during acid degradation of Ca-free AACs.

2. Materials and Experimental Methods

2.1 Materials

Metakaolin (MK) (MetaMax) was supplied by BASF Chemical Corporation (Georgia, USA). The chemical composition of MK, as determined by ICP-OES, is shown in **Table 1**. ICP-OES analysis was performed following the methodology reported in [21]. The alkali-activating solution used was prepared using sodium hydroxide (Sigma-Aldrich, NaOH ≥ 97%) and sodium silicate (Sigma-Aldrich, SiO_2 = 27 wt. %, Na_2O = 11 wt. %). Light metal (*i.e.*, Mg) addition to the AACs was provided in the form of brucite powder (Sigma-Aldrich, $Mg(OH)_2 \geq 95\%$). After the AAC pastes were created, the samples were exposed to a sulfuric acid solution with a pH of 2.0 ± 0.07. The sulfuric acid solutions were prepared by adding concentrated sulfuric acid (Sigma-Aldrich, $H_2SO_4 \geq 95\%$) to deionized water.

Table 1. Chemical composition of metakaolin in weight percentage (wt. %).

(wt.%)	**SiO_2**	**Al_2O_3**	**CaO**	**SO_4**	**Fe_2O_3**	**K_2O**	**Na_2O**	**P_2O_5**
Metakaolin	54%	47%	0.10%	0.30%	0.40%	0.10%	0.30%	0.10%

2.2 Experimental methods

The experiments were designed using a 2^2 factorial design of experiments. Specific proportions and constituent materials for each mixture design formulation (see **Table 2**) were selected based on ranges explored in previous studies. To enable the explicit study of MK-activated formulations that form faujasite minerals, the alkali (*i.e.,* sodium, Na) to aluminum ratio (Na:Al) was varied to produce cements with Na:Al ratios of 0.86 and 1.39. As previously elucidated by the authors in [21], Na:Al ratios of 1.39 and Si:Al ratios of 1.15 form faujasite minerals, while lower Na:Al ratios of 0.86 do not exhibit these mineral dynamics. Samples were prepared

without and with the addition of brucite to explore the effect of theis magnesium mineral on acid degradation of alkali-activated MK materials. In order to meet these Na:Al ratios and produce N-A-S-H binders during alkali-activation of MK the mass amounts of MK and alkali-activator solutions were not increased with brucite supplementation – a mineral admixture that remains inert during alkali-activation. However, it is important to note that the low liquid-to-solid ratio of brucite-supplemented samples resulted in poor workability and, as reported in [22] , presented less effective dispersion of raw materials. Workability issues were circumvented by employing high-shear mixing of all samples, as detailed in section 2.3. Brucite was added to obtain a Mg:Si ratio of 0.85, which was chosen based on previous research related to the synthesis of magnesium silicate hydrate (M-S-H) gels [23][16]. Such a high ratio studied herein result in a fundamental investigation of Mg chemical modification of the N-A-S-H binders present in alkali-activated MK materials.

Table 2. Mixture proportions for metakaolin-based alkali-activated cement control and $Mg(OH)_2$ addition samples.

Sample ID	**Constituent Materials**					**Important Parameters**		
Sample Name	MK (g)	$Mg(OH)_2$ (g)	NaSi (mL)	NaOH (g)	H_2O (ml)	Mg:Si	Si:Al	Na:Al
MK Control Low	50	0	13.5	13	45	0	1.15	0.86
MK Control High	50	0	13.5	22.8	45	0	1.15	1.39
Control Low + Mg	50	26.4	13.5	13	45	0.85	1.15	0.86
Control High + Mg	50	26.4	13.5	22.8	45	0.85	1.15	1.39

2.2.1 AAC sample preparation

AAC pastes were prepared using the calculated amounts of metakaolin, sodium silicate, sodium hydroxide, deionized water, and brucite ($Mg(OH)_2$) shown in **Such a** high ratio studied herein

result in a fundamental investigation of Mg chemical modification of the N-A-S-H binders present in alkali-activated MK materials.

Table 2. These components were mechanically mixed in a high-shear mixer for 3 minutes before being cast in molds (diameter 2.5 – 2.7 cm), after which the mixtures were tamped for 30 seconds and vibrated for 30 seconds. Paste samples were then cured in sealed containers (99% RH) in a Quincy forced air laboratory oven for 48 hours (2 days) at 40 °C. After initial curing, samples were demolded and cured 35 ± 5 °C for an additional 24 hours (1 day). These curing periods and temperature regimes were selected to control the mineral dynamics of metkaolin-based alkali-activated materials (i.e., extent of formation of faujasite minerals in MK control High and Control High + Mg samples) [21]. As a result, thermodynamic conditions were provided for Control High samples to form faujasites minerals, while Control Low samples retained a predominantly amorphous structure consisting of a N-A-S-H binder.

2.2.2 Acid exposure and leaching

Samples were exposed to a sulfuric acid solution (pH 2.0 ± 0.07) twice until pH equilibrium was attained, defined as $\Delta pH < 0.0025$ per hour. A modified ASTM C1308 methodology was employed to expose samples to acid. Modifications consisted of a volume-to-surface-area ratio of seven to determine the amount of acid solution to be used for each exposure as well as collection of the leachate only after pH equilibrium was attained. This pH-driven data collection ensures that information from complete acid-base reactions is collected and analyzed. Samples were suspended using a 46 mm Savillex support screen (730-0046) and stirred continuously in an acid solution using a magnetic stirrer to ensure homogenous solution mixing. Triplicates were utilized to ensure statistical robustness of the data. After pH equilibrium, leachate samples were collected, and acid solutions were replaced. Leachate samples were analyzed *via* ICP-OES and

ICP-MS. To account for brucite supplement by mass, the leaching data were normalized by the surface area of the cylindrical samples and cement content to facilitate comparison between samples.

2.2.3 Mineralogical characterization

Mineralogy was determined *via* semi-quantitative X-ray diffraction (XRD) using Cu Kα radiation (Siemens D500 X-ray diffractometer). An internal standard (*i.e.*, corundum, American Elements) was employed to normalize peak heights between samples and align diffraction patterns. Samples were homogenized by creating fine powders using a micronizing mill with well-packed yttrium-stabilized zirconium grinding beads. Subsequently, samples were homogenized in a plastic scintillation vial with three Delrin balls. 500 μL of Vertrel cleaning agent (Miller-Stephenson) was added to randomize particle orientation *via* the formation of aggregates. Lastly, samples were sieved through a 250 μm mesh and packed into XRD analysis plates. Samples were then analyzed from 5 to 65 degrees 2θ using Cu Kα X-ray radiation, with a step size of 0.02 degrees and a dwell time of 2 seconds per step. Diffraction patterns were analyzed using Jade software (MDI, Version 9) and the International Centre for Diffraction Data (ICDD) 2003 database.

2.2.4 Microstructural Mg:Al ratio determination

Electron microprobe analysis was employed using a JEOL JXA-8230 electron probe microanalyzer outfitted with five wavelength-dispersive spectrometers (WDS) and a Thermoscientific energy dispersive spectrometer (EDS) to examine the chemical composition of the AAC microstructure, namely changes in Mg:Al ratio upon acid exposure. The acceleration voltage and beam current used for all WDS acquisition was 15keV and 100nA, respectively. The pixel size chosen was 6 μm, and the electron beam was adjusted to match the size. Lastly, a

dwell time of 20 msec was used. The data were processed using CalcImage software (ProbeSoftware, Inc.) in order to apply the mean atomic number (MAN) background correction. EDS acquisition was standard-less using a spectral acquisition of 15 seconds, which was sufficient to accumulate counts over 4000. An acceleration voltage of 15 keV and a beam current of 20 nA was used for all acquisitions. An elemental matrix correction (ZAF) was performed in all acquisitions. Twenty randomized points were collected for five different locations in all samples (top, bottom, center, left, and right), totaling an acquisition of 100 EDS points per sample.

2.2.5 Nano- and micro-scale porosity determination

Nitrogen (N_2) adsorption using a Gemini V apparatus (Micromeritics) was used to characterize nano-scale gel porosity of unexposed and acid-exposed AAC samples. Identical sample formulations as those detailed in **Table 2** were prepared with unique sample sizes to fit test tubes (diameter: 0.65 cm, height: 1.4 cm) needed for N_2 adsorption experiments. Hence, materials were tested as a whole. All materials were first degassed for 24 hours in a vacuum (< 100 mTorr). For specific samples, duplicate measurements were collected. Porosities and pore-size distributions were calculated using the Barrett-Joyner-Hallenda (BJH) method prior to sulfuric acid exposure. Later, in order to characterize the unexposed micro-scale porosity, whole samples were subjected to X-ray micro-computed tomography (μ-CT) analysis in a Zeiss Xradia 520. Samples were secured in commercial plastic vials (diameter: 2.5 cm) and scanned using a 0.4x objective and X-ray source parameters of 60 kV acceleration voltage and 4 Watts. An air filter was utilized to reduce the transmission values between 29% and 60% and maintain intensity counts above 5000 by regulating the exposure time. A pixel size resolution of 5.786 microns was achieved utilizing a bin 1 pixel averaging acquisition.

177 Once the initial pore structure was characterized, samples were exposed to sulfuric acid
178 as detailed in section 2.2.2. The acid-attacked micro-scale pore structure was subsequently
179 characterized by μ-CT scans with the same settings as those stated previously. After μ-CT
180 scanning, the N_2 adsorption experiments employing the BJH method was conducted to
181 characterize the impact of acid exposure on the sample's nanoscale pore structure, as detailed
182 above. This procedure enabled the investigation of acid effects on both nano- and micro-scale
183 porosity for the whole sample, including both affected and unaffected areas.
184 All μ-CT scans were reconstructed using the ZEISS Scout-and-Scan Control System
185 Reconstructor (V.11.1.6411.17883) software to manually adjust the center shift values and
186 minimize beam hardening artifacts. Prior to pore-structure segmentation, image pre-processing in
187 Dragonfly 4.0 was required to minimize noise from acidic solutions. Denoising and smoothing
188 were performed utilizing an Open mathematical morphology operation (circle kernel size of 7), a
189 median smoothing (circle kernel size of 3), and a non-local means smoothing (square kernel size
190 of 9). Such a procedure enabled consistent segmentation across all scans.

191 ## 3. Results and Analysis

192 ### 3.1 Physical Evidence of Sulfuric Acid Degradation

193 The addition of brucite visibly improved the pH ~2 acid resistance of the AAC formulations
194 investigated herein, as visually demonstrated in **Figure 1**. Failure of control formulations without
195 brucite addition was evident at both alkali contents, indicating a greater extent of binder
196 breakdown by sulfuric acid attack in those samples. While structural integrity was maintained in
197 Control Low + Mg samples, shallow surface cracks were observed, indicating some surface-level
198 degradation. However, Control High + Mg samples maintained structural integrity and exhibited

no observable cracking, suggesting that brucite addition improved the sulfuric acid resistance of the high-alkali sample.

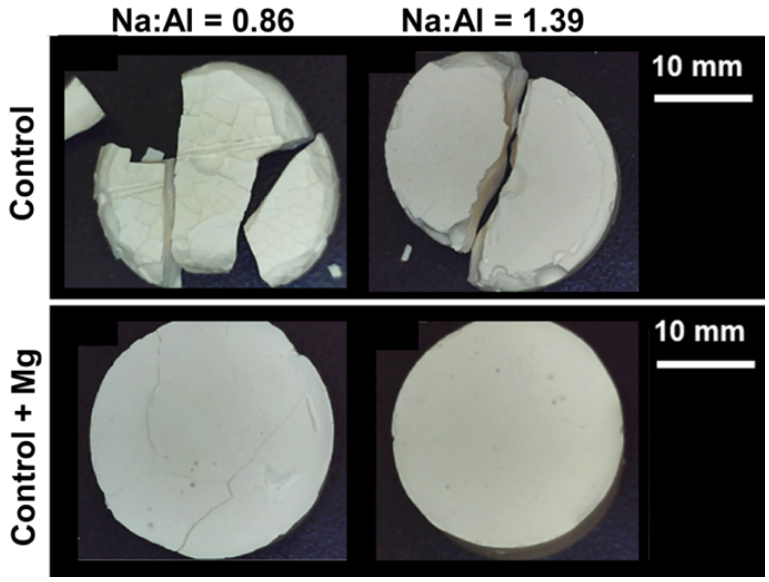

Figure 1. Visual evidence of a sulfuric acid attack on Ca-free AACs for representative non-supplemented samples (control) and supplemented samples with brucite (control + Mg).

3.2 Chemical Evidence of Sulfuric Acid Degradation

Brucite addition increased elemental silicon (Si) retention upon acid exposure, as demonstrated by a reduced loss (*i.e.*, reduced leaching) of Si (see **Table 3**). Low Na:Al samples with brucite revealed negligible differences during the first acid exposure but a 75% decrease during the second acid exposure. Incorporation of brucite in higher Na:Al content formulations (Control High samples) decreased Si leaching 35% and 75% of during the first and second acid exposure cycles, respectively. However, the concentration of leached Si remained high in these formulations and is observed to correlate well with sodium (Na) leaching. This result can be explained by the presumed existence of Si monomers and dimers in the pore solution, which can

polymerize and gelate *via* Na stabilization. Recent studies of Na:Al = 1.0 AACs have found an increased content of orthosilicic acid (*i.e.*, Si monomers) 15 hours after alkali-activation [24,25]. This increase in monomeric Si concentration enables the formation of silica gel networks within the perimeter of the sample—a well-known phenomenon of AACs [2,11,26,27].

The addition of brucite improved the acid resistance of AACs by reducing dealumination of the Si-O-Al bonds in the N-A-S-H binder. Upon first acid exposure, regardless of brucite addition or alkali content, dealumination and magnesium (Mg) leaching is minimal for both formulations that contain Mg (**Table 3**). However, upon second acid exposure, dealumination increased in samples without brucite. Increased dealumination occurs concomitantly with a decrease in Na leaching, indicating that the electrophilic attack of protons cannot be arrested solely by the alkalinity within the AAC. Contrastingly, samples containing brucite release Mg, indicating that the dissolution of brucite aids in increasing the alkalinity (*i.e.*, pH buffering capacity) of these formulations. High Na:Al samples with brucite are observed to retain dissolved Mg and simultaneously exhibit lower dealumination. These results chemically support the physical evidence observed in **Figure 1** that brucite improves the acid resistance of AACs, especially at high alkali contents.

Table 3. Normalized elemental leaching for all samples for both first and second acid exposure after achieving pH equilibrium.

	1st Equilibrium							
	MK Control Low		**Control Low + Mg**		**MK Control High**		**Control High + Mg**	
	mean	*s.d.*	*mean*	*s.d.*	*mean*	*s.d.*	*mean*	*s.d.*
Si	0.05	0.007	0.05	0.004	1.61	0.034	0.96	0.068
Al	0.16	0.010	0.03	0.002	0.04	0.005	0.04	0.014

Na	7.96	0.135	6.45	1.505	15.02	0.422	12.87	2.776
Mg	-	-	0.02	0.006	-	-	0.00	0.001

	2nd Equilibrium							
	MK Control Low		**Control Low + Mg**		**MK Control High**		**Control High + Mg**	
	mean	*s.d.*	*mean*	*s.d.*	*mean*	*s.d.*	*mean*	*s.d.*
Si	0.45	0.037	0.16	0.037	0.44	0.003	0.13	0.006
Al	0.06	0.054	0.00	0.000	0.05	0.039	0.00	0.000
Na	2.11	0.236	2.38	0.386	2.16	0.109	2.95	0.426
Mg	-	-	0.30	0.055	-	-	0.03	0.020

Mineralogies of Control and Control + Mg samples before and after acid exposure remain unchanged between formulations (see **Figure 2**), indicating that no significant precipitation reactions occurred during acid exposure. All samples indicate a predominantly amorphous component, identified by a hump ~25° 2θ angles. This amorphous component is indicative of N-A-S-H. Silicon-rich faujasite minerals ($Na_{2.06}Al_2Si_{3.8}O_{11.63}\cdot 8H$) form in high sodium content (Na:Al = 1.39) formulations, regardless of brucite addition, as expected [21]. Upon acid exposure, minimal changes in the mineralogy of AACs are observed. High Na:Al samples demonstrated an increased diffraction intensity of faujasite after acid exposure, possibly indicating further mineralization during acid exposure. Similar mineralization reactions after acidic exposure observed by [28] were also correlated to reduced porosity and increased mechanical performance. Thus, these results indicate that acid degradation of these Ca-free AACs does not involve significant precipitation reactions as observable in Ca-rich cementitious materials, which form gypsum (*e.g.*, $CaSO_4\cdot 2H_2O$) phases upon exposure to sulfuric acid [29,30].

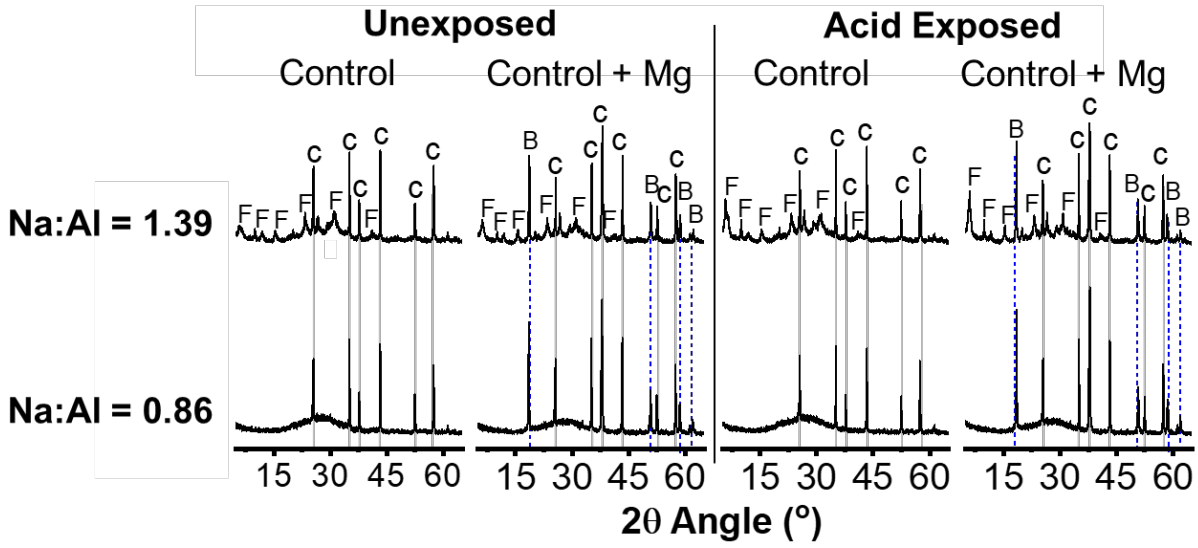

248

249 **Figure 2.** Mineralogy of AAC samples without and with brucite before and after acid exposure.
250 Symbols correspond to mineral phases identified as follows: "F" indicates the presence of
251 faujasite-Na ($Na_{2.06}Al_2Si_{3.8}O_{11.63}\cdot 8H_2O$); "B" indicates the presence of brucite ($Mg(OH)_2$); and,
252 "C" indicates the presence of corundum (Al_2O_3), which was used as an internal standard.

253 The acid neutralization capacity of AACs increases with the addition of brucite during
254 the second acid exposure (**Figure 3**). Brucite-supplemented samples attained higher equilibrium
255 pH values indicating a higher acid neutralization capacity than their control counterparts. During
256 the first acid exposure, regardless of alkali content, equilibrium pH values of all samples are not
257 statistically different (p-value of 0.517). As discussed earlier in regard to leaching data (**Table**
258 **3**), pH values are highly correlated with an increase in Na leaching during the first acid exposure.
259 The correlation was verified by computing the Pearson correlation coefficient, which yielded a
260 value of 0.938 (p-value of 0.0001). This correlation is expected, given that an inter-cationic
261 exchange between H^+ and Na occurs during the first step of acid degradation of N-A-S-H. Also,
262 the acid-base reaction of trace carbonates and hydroxides in the pore solution (e.g., Na_2CO_3,

NaOH) may contribute to this leaching correlation. However, the presence of these phases in the pore solution is speculated as XRD was unable to resolve distinct patterns in the solid phase of these materials (**Figure 2**). Remnant NaOH is evidenced by high equilibrium pH values (*i.e.*, 12.4, 12.7) attained in high Na-content formulations (Na:Al = 1.39). However, during the second acid exposure, samples without brucite demonstrated a low acid neutralization capacity, achieving equilibrium pH < 4.6. The addition of brucite improves acid neutralization capacity. Control Low + Mg and Control High + Mg samples reach pH values of 10.2 and 7.0, respectively, during the second acid exposure.

It is worth noting that, while Control High + Mg samples attain lower pH equilibrium conditions, these samples simultaneously demonstrate high Mg retention (**Figure 2**), which indicate differences in acid-base reactions occurring in the samples. In order to explain the differences in the acid-base reactions occurring in the pastes, a microstructural chemical analysis was performed. More specifically, Mg:Al ratios of the pastes were determined before and after exposure to acid. While Control Low + Mg formulations exhibited higher acid neutralization capacity, Control High + Mg samples were evidently more acid resistant.

The high Na:Al samples with brucite exhibit a two-fold increase in Mg:Al ratio within their microstructures after the second acid exposure (**Figure 4**). The increase of Mg and Al spatial pairing is likely a result of Mg stabilization of negative moieties along with the acid-attacked Si-O-Al bonds – a process name *polyvalent cationic stabilization* and previously hypothesized in [17]. Contrastingly, Control Low + Mg samples demonstrate lower Mg:Al ratios after acid exposure a consequence of high Mg leaching (**Table 3**). This observed leaching of alkalis (e.g., Na, Mg, K, Ca) is a common phenomenon that has been previously observed in AACs [31–33].

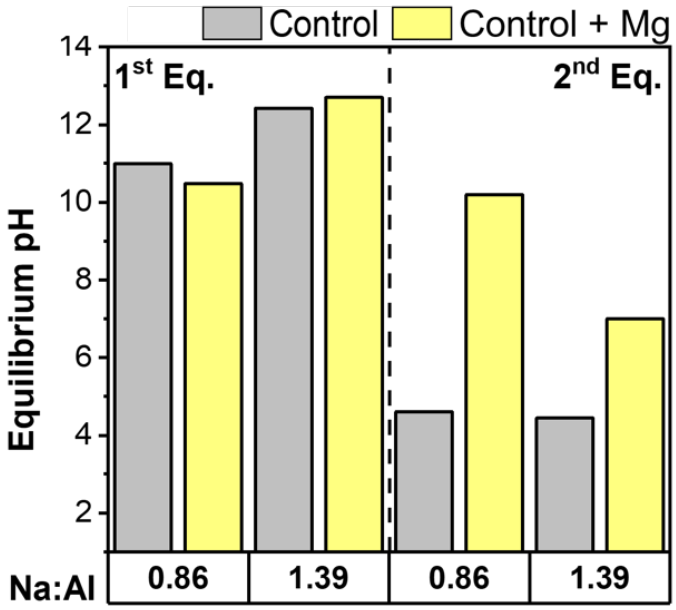

286

287 **Figure 3.** Equilibrium pH of sulfuric acid solutions for samples without and with brucite. Data
288 show pH of the leachate after the first and second acid equilibrium exposure cycles.

289 Polyvalent cationic stabilization of negative moieties in the N-A-S-H binder can occur
290 due to functionalized brucite surfaces or release of Mg^{2+} cations. Seminal research on Brucite
291 ($Mg(OH_2)$) surface chemistry has shown that the protonation of the mineral surface (>Mg-OH)
292 yields $>MgOH_2^+$ sites, which are at a maximum concentration on brucite surfaces at pH values <
293 7.0. As observed in **Figure 3**, the final equilibrium pH of Control High + Mg samples is 7.0,
294 which may enable dipole-dipole interactions between $>MgOH_2^+$ and negative moieties of the
295 surrounding N-A-S-H binder [34]. Additionally, $>MgOH_2^+$ surface sites also enable the
296 dissolution and release of Mg^{2+} ions, according to the thermodynamically preferred dissolution
297 reaction (pike -16.844) [35,36]:

298

299 $$Mg(OH)_2 + 2H^+ \rightarrow Mg^{2+} + 2H_2O$$

300 Eq. 1

301

302 Lastly, the small atomic radii of Mg^{2+} ions are advantageous in terms of mobility, which would

303 facilitate leaching. However, results presented here suggest a higher retention of Mg^{2+} due to

304 Mg-Al interactions in the high Na:Al samples with brucite. Thus, it is evident that a higher

305 number of Mg-Al interactions within the AAC microstructure yield improved acid resistance

306 with a lower breakdown of the Si-O-Al bonds of N-A-S-H binders

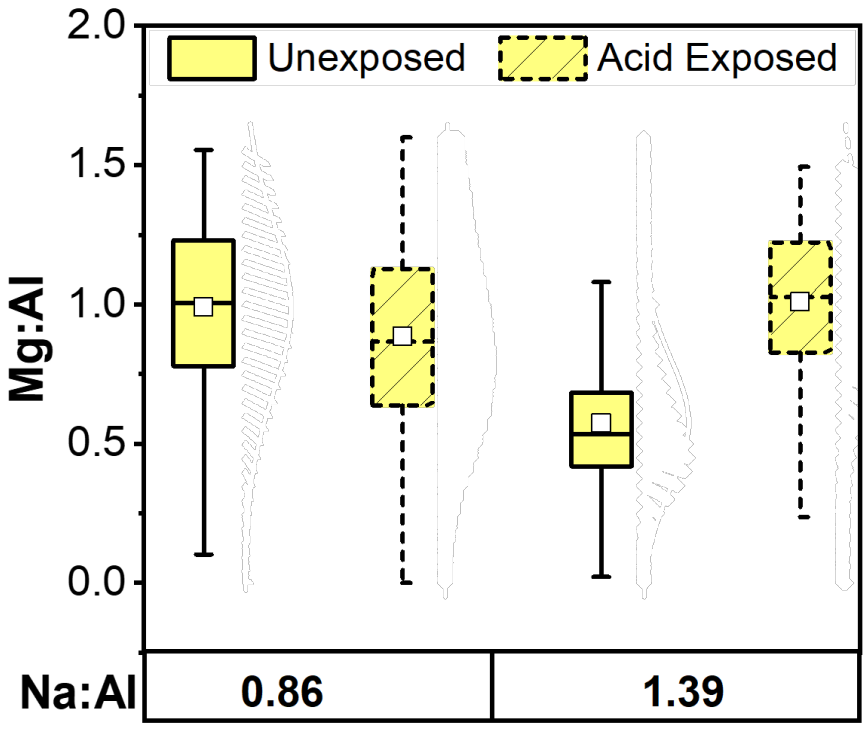

307

308 **Figure 4.** Distribution and mean atomic Mg:Al ratio of Control Low + Mg (Na:Al = 0.86) and

309 Control High + Mg (Na:Al = 1.39) AAC samples before and after acid exposure.

3.3 Porosity of Alkali-Activated Cements Supplemented with Brucite

Micro-scale porosities of all samples before and after acid exposure are shown in **Figure 5**. Non-connected porosities between 0.3%-0.8% are comparable to those reported by X-ray microtomography (μCT) studies of other fly ash-based AACs [37,38]. Results in **Figure 5** demonstrate that the addition of brucite at high Na:Al formulations decrease by 18% the porosity of AACs, while the opposite effect is observed at low Na:Al formulations containing brucite demonstrating a 26% porosity increase.

As observed in **Figure 5,** increased alkali-content results in higher porosity values as observed for Control High formulations. This is a dissimilar trend reported in other AAC literature, where increased Na content is expected to decrease porosity due to an increased formation of reaction products and a denser microstructure [39]. Observed porosity differences, although minor, may be explained by utilization of activating solutions with low silica modulus (Ms) values (Ms = 0.27) at high Na:Al formulations [40]. These activating solutions have higher viscosities due to higher contents of dissolved Na and Si ions and, hence, an increase of porosity is anticipated as a consequence of entrapped air during mixing [41–43]. This likely results in decreased compressive strength, due to a lower bulk density associated with higher porosities in less workable mixes [44].

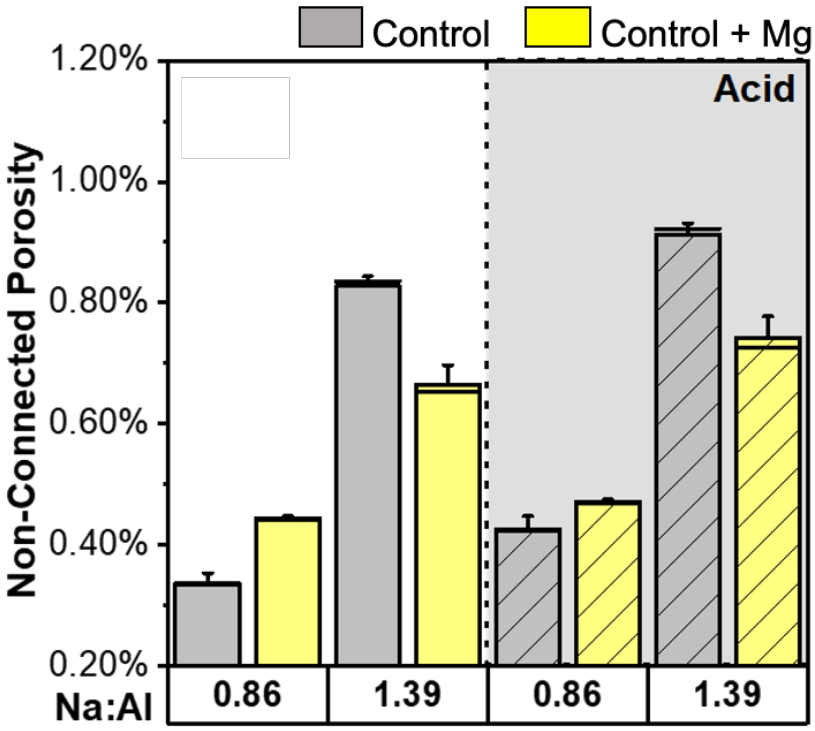

Figure 5. μ-CT non-connected porosities of all AAC samples before and after the first sulfuric acid exposure (pH of 2.0 ±0.07).

Regardless of brucite addition, AACs develop higher micro-scale porosities during the first acid exposure. The addition of brucite reduces the increase in porosity for both Control Low and Control High formulations by 50.9% and 14.1%, respectively. These results correlate well with the lower Na and Si leaching of these samples (**Table 3**). The expected Si gelation and retention of Na ions likely plays a role in decreasing the changes in porosity at the micro-scale of brucite-supplemented AACs. Moreover, results suggest that the preservation of the pore structure in Control Low + Mg samples correlates with reduced dealumination. In light of the Mg:Al results shown in **Figure 4**, as well as leaching results presented in **Table 3**, Control High + Mg samples may preserve their porous structure as a result of Mg-Al stabilization. The formation of

crystalline faujasite phases during acid attack, as discussed in **Figure 2**, may also play a role in pore-structure preservation.

Addition of brucite in low Na:Al formulations is observed to double the gel pore volumes above a pore size of 10 nm (**Figure 6**). In general, the opposite trend is observed at high Na:Al formulations with brucite (Control High + Mg) as these samples exhibit a ~30% lower nano-scale porosity when compared to samples without brucite. Moreover, when analyzing the effect of alkali content, Control High formulations have a higher content of nano-scale porosity, when compared to Control Low. These nano-scale porosity trends are consistent with the micro-scale porosity trends observed in **Figure 5**. Increased micro- and nano-scale porosity at higher sodium contents may be due to residual inter-layer porosity from unreacted MK precursor, as well as rheology differences due to extent of binder network formation, as previously discussed [45].

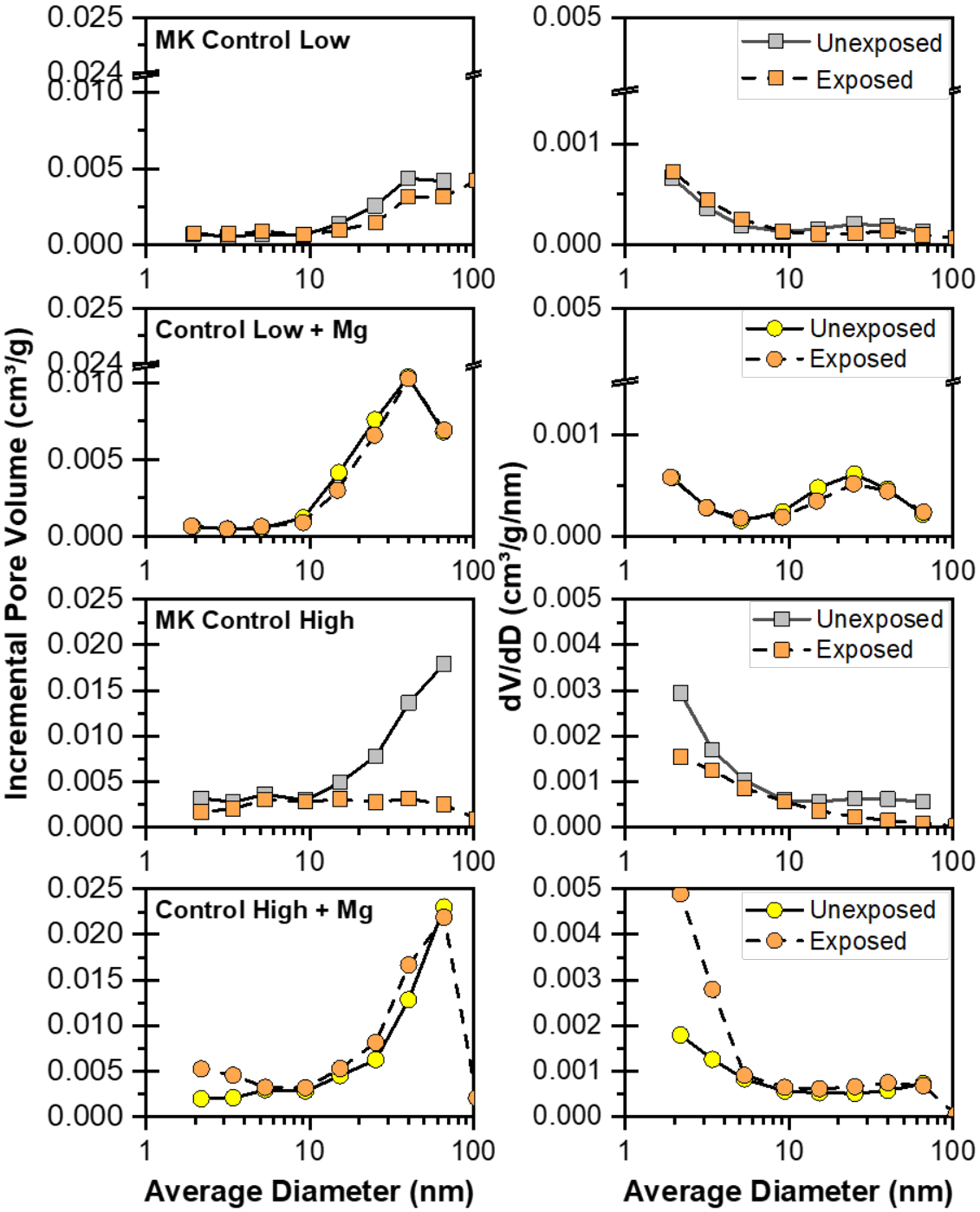

350

351 **Figure 6.** Nano-scale porosity characterization of all samples without and with brucite addition

352 before acid exposure and after sulfuric acid exposure (pH of 2.0 ±0.07).

353

Upon acid exposure, there is an apparent decrease in incremental pore volume in samples without brucite, see **Figure 6**. Given the utilization of BJH, the apparent decrease in nano-scale pore volume may actually be a consequence of acidic dissolution, which may create larger pores (> 100 nm) outside of the method's pore size range. This result is supported by a higher extent of Si-O-Al breakdown as shown by high leaching of Na, Si, and Al (**Table 3**) as well as the increased micro-scale porosity (**Figure 5**).

Nonetheless, it is evident that the addition of brucite preserves nano-scale porosity. Interestingly, only Control High formulations with brucite double in nano-scale porosity (< 5nm), which may increase the tortuosity of porous network and, hence, increase the dissolution of brucite. Similar observable increases in tortuosity have been reported in previous experiments with chemically-active mineral admixtures [46]. As Mg^{2+} ions are liberated from the acid-induced dissolution of brucite, the higher tortuosity may increase the probability of Mg^{2+} encountering negative moieties along the acid-attack N-A-S-H binder. This phenomenon could suggest a higher Mg retention (**Table 3**) and concomitant lower acid neutralization capacity (**Figure 3**), which would lead to increased Mg-Al pairing within the microstructure (**Figure 4**). Together, these results indicate that the increase in tortuosity caused by an increase in nano-scale gel pores after acid exposure may be critical to the effectiveness of the polyvalent cationic stabilization mechanism.

4. Conclusions

We studied the effect of brucite, a common mineral found in unreacted and reacted AAC materials, on the sulfuric acid resistance of alkali-activated metakaolin. Converging lines of evidence suggest that brucite improves acid resistance by (1) increasing acid neutralization capacity and/or (2) polyvalent cationic stabilization, depending on AAC formulation.

Experimental data indicate that brucite increases acid resistance in AACs with low alkali contents (Na:Al = 0.86) by increasing acid neutralization capacity alone. Low Na:Al AACs with brucite exhibit a high acid neutralization capacity, with equilibrium pH values reaching >10 after the first and second acid exposure. This neutralization, in turn, resulted in decreased loss of Al, Si, and Na upon acid exposure, indicating a reduced breakdown of Si-O-Al. The decreased leaching of Al, Si, and Na also correlated with minimal changes to micro-scale preservation of nano-scale porosity (1-100 nm). However, no significant changes in Mg-Al pairing were observed in these samples and, as a result, polyvalent cationic stabilization was not evidenced in these samples.

Experimental data also indicate that brucite improves acid resistance in AACs with high alkali (Na:Al = 1.39) contents by increasing acid neutralization capacity *and* polyvalent cationic stabilization. Upon acid exposure, addition of brucite improved acid resistance, as evidenced by lower Al, Si, and Na leaching and simultaneous increases in acid neutralization capacity compared samples without brucite. However, the acid neutralization capacity was dependent on Mg leaching and, during the second acid exposure, Mg was retained within the material's microstructure. This retention led to a decrease in the acid neutralization capacity and a concomitant increase in Mg-Al interactions, as evinced *via* electron microprobe analysis. Results also demonstrate that, while the nano-scale porous structure was preserved in these samples, there was an increase in pore sizes <5nm. Increased nano-scale porosity likely increased the tortuosity and brucite dissolution, which supports the increase in Mg-Al pairing observed. Together, these results provide evidence in support of polyvalent cationic stabilization as a

unique acid resistance mechanism that preserves the integrity of aluminosilicate binders upon exposure to acid.

5. References

[1] Roy D M, Alkali activated cements, opportunities and challenges, Cem. Concr. Res. 29 (1999) 249–254.

[2] B. Singh, G. Ishwarya, M. Gupta, S.K. Bhattacharyya, Geopolymer concrete: A review of some recent developments, Constr. Build. Mater. 85 (2015) 78–90. https://doi.org/10.1016/J.CONBUILDMAT.2015.03.036.

[3] J. Provis, Geopolymers and other alkali activated material: why, how, what? , Mater. Struct. 47 (2013) 25.

[4] L. Struble, E. Kim, L. Gomez-Zamorano, Overview of Geopolymer cement, (2013).

[5] P. Duxson, a. Fernández-Jiménez, J.L. Provis, G.C. Lukey, a. Palomo, J.S.J. van Deventer, Geopolymer technology: the current state of the art, J. Mater. Sci. 42 (2007) 2917–2933. https://doi.org/10.1007/s10853-006-0637-z.

[6] J.L. Provis, A. Palomo, C. Shi, Advances in understanding alkali-activated materials, Cem Concr Res. 78 (2015) 110–125. https://doi.org/10.1016/j.cemconres.2015.04.013.

[7] A. Fernandez-Jimenez, A. Palomo, Chemical durability of Geopolymers, in: J.L. Provis, J. Van Deventer (Eds.), Geopolymers- Struct. Process. Prop. Ind. Appl., 2009: pp. 167–193.

[8] A. Allahverdi, F. Skvara, Acidic corrosion of hydrated cement based materials. Part 1. Mechanism of the Phenomenon, Ceram.-Silikáty. 44 (2000) 152–160.

[9] T. Bakharev, J.G. Sanjayan, Y.B. Cheng, Resistance of alkali-activated slag concrete to acid attack, Cem. Concr. Res. 33 (2003) 1607–1611. https://doi.org/10.1016/S0008-8846(03)00125-X.

[10] F. Pacheco-Torgal, J. Castro-Gomes, S. Jalali, Alkali-activated binders: A review. Part 1. Historical background, terminology, reaction mechanisms and hydration products, Constr. Build. Mater. 22 (2008) 1305–1314. https://doi.org/10.1016/j.conbuildmat.2007.10.015.

[11] T. Bakharev, Resistance of geopolymer materials to acid attack, Cem. Concr. Res. 35 (2005) 658–670. https://doi.org/10.1016/j.cemconres.2004.06.005.

[12] C. Grengg, F. Mittermayr, N. Ukrainczyk, G. Koraimann, S. Kienesberger, M. Dietzel, Advances in concrete materials for sewer systems affected by microbial induced concrete corrosion: A review, Water Res. 134 (2018) 341–352. https://doi.org/10.1016/j.watres.2018.01.043.

[13] R.J. Myers, B. Lothenbach, S.A. Bernal, J.L. Provis, Thermodynamic modelling of alkali-activated slag cements, Appl. Geochem. 61 (2015) 233–247. https://doi.org/10.1016/J.APGEOCHEM.2015.06.006.

[14] C.-L. Hwang, D.-H. Vo, V.-A. Tran, M.D. Yehualaw, Effect of high MgO content on the performance of alkali-activated fine slag under water and air curing conditions, Constr. Build. Mater. 186 (2018) 503–513. https://doi.org/10.1016/J.CONBUILDMAT.2018.07.129.

[15] T. Yang, X. Yao, Z. Zhang, Geopolymer prepared with high-magnesium nickel slag: Characterization of properties and microstructure, Constr. Build. Mater. 59 (2014) 188–194. https://doi.org/10.1016/J.CONBUILDMAT.2014.01.038.

[16] X. Huang, S. Hu, F. Wang, Y. Liu, Y. Mu, Properties of alkali-activated slag with addition of cation exchange material, Constr. Build. Mater. 146 (2017) 321–328. https://doi.org/10.1016/j.conbuildmat.2017.03.127.

[17] J.P. Gevaudan, A. Caicedo-Ramirez, M.T. Hernandez, W. V. Srubar, Copper and cobalt improve the acid resistance of alkali-activated cements, Cem. Concr. Res. 115 (2018) 1–12. https://doi.org/10.1016/j.cemconres.2018.08.002.
[18] T. Yang, Z. Zhang, H. Zhu, X. Gao, C. Dai, Q. Wu, Re-examining the suitability of high magnesium nickel slag as precursors for alkali-activated materials, Constr. Build. Mater. 213 (2019) 109–120. https://doi.org/10.1016/j.conbuildmat.2019.04.063.
[19] M.X. Peng, Z.H. Wang, Q.G. Xiao, F. Song, W. Xie, L.C. Yu, H.W. Huang, S.J. Yi, Effects of alkali on one-part alkali-activated cement synthesized by calcining bentonite with dolomite and Na2CO3, Appl. Clay Sci. 139 (2017) 64–71. https://doi.org/10.1016/j.clay.2017.01.020.
[20] R.J. Myers, S.A. Bernal, J.L. Provis, Phase diagrams for alkali-activated slag binders, Cem. Concr. Res. 95 (2017) 30–38. https://doi.org/10.1016/j.cemconres.2017.02.006.
[21] J.P. Gevaudan, K.M. Campbell, T.J. Kane, R.K. Shoemaker, W. V. Srubar, Mineralization dynamics of metakaolin-based alkali-activated cements, Cem. Concr. Res. 94 (2017) 1–12. https://doi.org/10.1016/j.cemconres.2017.01.001.
[22] X. Gao, Q.L. Yu, H.J.H. Brouwers, Assessing the porosity and shrinkage of alkali activated slag-fly ash composites designed applying a packing model, Constr. Build. Mater. 119 (2016) 175–184. https://doi.org/10.1016/j.conbuildmat.2016.05.026.
[23] D. Nied, K. Enemark-rasmussen, E.L. Hopital, J. Skibsted, B. Lothenbach, Properties of magnesium silicate hydrates (M-S-H), Cem. Concr. Res. 79 (2016) 323–332.
[24] P. Duxson, G.C. Lukey, F. Separovic, J.S.J. Van Deventer, Effect of Alkali Cations on Aluminum Incorporation in Geopolymeric Gels, (2005) 832–839.
[25] X. Chen, A. Sutrisno, L. Zhu, L.J. Struble, Setting and nanostructural evolution of metakaolin geopolymer, J. Am. Ceram. Soc. 100 (2017) 2285–2295.
[26] F. Pacheco-Torgal, Z. Abdollahnejad, a. F. Camões, M. Jamshidi, Y. Ding, Durability of alkali-activated binders: A clear advantage over Portland cement or an unproven issue?, Constr. Build. Mater. 30 (2012) 400–405. https://doi.org/10.1016/j.conbuildmat.2011.12.017.
[27] O. Burciaga-Díaz, J.I. Escalante-García, Strength and Durability in Acid Media of Alkali Silicate-Activated Metakaolin Geopolymers, J. Am. Ceram. Soc. 95 (2012) 2307–2313. https://doi.org/10.1111/j.1551-2916.2012.05249.x.
[28] A. Palomo, M.T.T. Blanco-Varela, M.L.L. Granizo, F. Puertas, T. Vazquez, M.W.W. Grutzeck, Chemical stability of cementitious materials based on metakaolin, Cem. Concr. Res. 29 (1999) 997–1004. https://doi.org/10.1016/S0008-8846(99)00074-5.
[29] C. Grengg, N. Ukrainczyk, G. Koraimann, B. Mueller, M. Dietzel, F. Mittermayr, Long-term in situ performance of geopolymer, calcium aluminate and Portland cement-based materials exposed to microbially induced acid corrosion, Cem. Concr. Res. 131 (2020) 106034. https://doi.org/10.1016/j.cemconres.2020.106034.
[30] P. Sturm, G.J.G. Gluth, C. Jäger, H.J.H. Brouwers, H.-C. Kühne, Sulfuric acid resistance of one-part alkali-activated mortars, Cem. Concr. Res. 109 (2018) 54–63. https://doi.org/10.1016/j.cemconres.2018.04.009.
[31] F.F. Škvára, V.V. Šmilauer, P. Hlaváček, L. Kopecký, Z. Cílová, P. Hlavácek, L. Kopecky, Z. Cilová, A Weak Alkali Bond in (N,K)-A-S-H Gels: Evidence from Leaching and Modeling, Ceram. − Silikáty. 56 (2012) 374–382.
[32] P.-T. Fernando, J. Said, Resistance to acid attack, abrasion and leaching behavior of alkali-activated mine waste binders, Mater. Struct. 44 (2011) 487–498. https://doi.org/10.1617/s11527-010-9643-3.
[33] M. Mustafa Al Bakri Abdullah, H. Kamarudin, A. Victor Sandu Gheorghe Asachi, C. Mohd Ruzaidi, M. Al Bakri Abdullah, Sulfuric Acid Attack on Ordinary Portland Cement and Geopolymer Material, n.d.

[34] O.S. Pokrovsky, J. Schott, Experimental study of brucite dissolution and precipitation in aqueous solutions: surface speciation and chemical affinity control, Geochim. Cosmochim. Acta. 68 (2004) 31–45. https://doi.org/10.1016/S0016-7037(03)00238-2.
[35] J.W. Johnson, E.H. Oelkers, H.C. Helgeson, SUPCRT92: A software package for calculating the standard molal thermodynamic properties of minerals, gases, aqueous species, and reactions from 1 to 5000 bar and 0 to 1000°C, Comput. Geosci. 18 (1992) 899–947. https://doi.org/10.1016/0098-3004(92)90029-Q.
[36] E.H. Oelkers, P. Benezeth, G.S. Pokrovski, Thermodynamic Databases for Water-Rock Interaction, Rev. Mineral. Geochem. 70 (2009) 1–46. https://doi.org/10.2138/rmg.2009.70.1.
[37] J.L. Provis, R.J. Myers, C.E. White, V. Rose, J.S.J.J. Van Deventer, X-ray microtomography shows pore structure and tortuosity in alkali-activated binders, Cem. Concr. Res. 42 (2012) 855–864. https://doi.org/10.1016/j.cemconres.2012.03.004.
[38] S. Das, P. Yang, S.S. Singh, J.C.E. Mertens, X. Xiao, N. Chawla, N. Neithalath, Effective properties of a fly ash geopolymer: Synergistic application of X-ray synchrotron tomography, nanoindentation, and homogenization models, Cem. Concr. Res. 78 (2015) 252–262. https://doi.org/10.1016/J.CEMCONRES.2015.08.004.
[39] D. Ravikumar, S. Peethamparan, N. Neithalath, Structure and strength of NaOH activated concretes containing fly ash or GGBFS as the sole binder, Cem. Concr. Compos. 32 (2010) 399–410. https://doi.org/10.1016/J.CEMCONCOMP.2010.03.007.
[40] D.W. Law, A.A. Adam, T.K. Molyneaux, I. Patnaikuni, Durability assessment of alkali activated slag (AAS) concrete, Mater. Struct. 45 (2012) 1425–1437. https://doi.org/10.1617/s11527-012-9842-1.
[41] A. Favier, J. Hot, G. Habert, N. Roussel, J.-B. d'Espinose de Lacaillerie, Flow properties of MK-based geopolymer pastes. A comparative study with standard Portland cement pastes, Soft Matter. 10 (2014) 1134–1141.
[42] P. Chindaprasirt, T. Chareerat, V. Sirivivatnanon, Workability and strength of coarse high calcium fly ash geopolymer, Cem. Concr. Compos. 29 (2007) 224–229. https://doi.org/10.1016/j.cemconcomp.2006.11.002.
[43] K.L. Aughenbaugh, T. Williamson, M.C.G. Juenger, Critical evaluation of strength prediction methods for alkali-activated fly ash, Mater. Struct. 48 (2015) 607–620. https://doi.org/10.1617/s11527-014-0496-z.
[44] Y.M. Liew, H. Kamarudin, A.M. Mustafa Al Bakri, M. Bnhussain, M. Luqman, I. Khairul Nizar, C.M. Ruzaidi, C.Y. Heah, Optimization of solids-to-liquid and alkali activator ratios of calcined kaolin geopolymeric powder, Constr. Build. Mater. 37 (2012) 440–451. https://doi.org/10.1016/J.CONBUILDMAT.2012.07.075.
[45] P.S. Das, M. Bhattacharya, D.K. Chanda, S. Dalui, S. Acharya, S. Ghosh, A.K. Mukhopadhyay, Failure and deformation mechanisms at macro- and nano-scales of alkali activated clay, J. Phys. Appl. Phys. 49 (2016) 235503. https://doi.org/10.1088/0022-3727/49/23/235503.
[46] N.R. Rakhimova, R.Z. Rakhimov, Reaction products, structure and properties of alkali-activated metakaolin cements incorporated with supplementary materials – a review, J. Mater. Res. Technol. (2018). https://doi.org/10.1016/J.JMRT.2018.07.006.